https://doi.org/10.5194/egusphere-2025-56
Preprint. Discussion started: 10 February 2025

Evolution of tropospheric aerosols over central China during 2010-2024 as observed by lidar

Dongzhe Jing[1,2,3], Yun He[1,2,3,*], Zhenping Yin[4], Kaiming Huang[1,2,3], Fuchao Liu[1,2,3], Fan Yi[1,2,3]

[1]School of Earth and Space Science and Technology, Wuhan University, Wuhan 430072, China
[2]Key Laboratory of Geospace Environment and Geodesy, Ministry of Education, Wuhan 430072, China.
[3]State Observatory for Atmospheric Remote Sensing, Wuhan 430072, China.
[4]School of Remote Sensing and Information Engineering, Wuhan University, Wuhan 430072, China.

**Correspondence to:* Yun He (heyun@whu.edu.cn)

Abstract. Air quality in China has improved significantly over the past decade. However, recent studies show that this progress has notably slowed in recent years. To investigate regional patterns and driving factors, we examined the long-term evolution of tropospheric aerosols over Wuhan (30.5°N, 114.4°E) from 2010 to 2024, using ground-based polarization lidar observations. Aerosol optical depth (AOD) trends are divided into two phases: a declining trend (-0.077 yr^{-1}) during 2010-2017 (stage I) and a fluctuating period during 2018-2024 (stage II). Contributions from natural (dust) and anthropogenic (non-dust) aerosols were analyzed separately. Dust optical depth (DOD) consistently declined (-0.011 yr^{-1}) until August 2020 and became larger again afterwards. In stage I, anthropogenic aerosols (-0.068 yr^{-1}) were responsible for 88.3% of the total AOD reduction, primarily due to decreases in boundary-layer AOD. In stage II, anthropogenic AOD fluctuated, possibly due to atmospheric chemistry factors. Seasonal variations were also observed. Anthropogenic aerosols appeared from surface to 2.5 km in summer, with particle extinction and mass concentration of 0.12 km^{-1} and 83.0 μg m^{-3}, which were concentrated below 0.7 km in winter, with much higher particle extinction and mass concentration of 0.31 km^{-1} and 211.8 μg m^{-3}. Two case studies highlighted typical pollution events: summertime transboundary agricultural biomass burning smoke in June 2014 and wintertime local anthropogenic aerosol pollution in January 2019. These findings improve our understanding of how regional aerosols respond to local emission controls and long-range transport of dust and smoke.

https://doi.org/10.5194/egusphere-2025-56
Preprint. Discussion started: 10 February 2025

1 Introduction

Atmospheric aerosols play an essential role in the global climate by affecting the radiation budget through the absorption or scattering of solar radiation (Huang et al., 2014; Bellouin et al., 2020; Liu and Matsui, 2021). In addition, aerosols act as cloud condensation nuclei or ice nucleating particles, significantly influencing cloud properties through aerosol-cloud interactions (ACI) (Rosenfeld et al., 2014; Kanji et al., 2017; Yin et al., 2021a; He et al., 2021, 2022a). ACI processes currently contribute the largest uncertainty in global effective radiation forcing (IPCC, 2021). Furthermore, aerosols are closely linked to the living environment and human health. Particulate matter with a diameter <2.5 μm ($PM_{2.5}$) is one of the most important air pollutants, capable of being inhaled into the lungs, thereby degrading air quality, reducing visibility, and damaging human health (van Donkelaar et al., 2015; Cohen et al., 2017).

During the first decade of the 21st century, rapid urbanization and industrialization in China caused severe air pollution, leading to a significant increase in $PM_{2.5}$ concentrations and aerosol optical depth (AOD) (Xie et al., 2016; Hu et al., 2021a; de Leeuw et al., 2022). To address this issue, the Chinese government implemented the "*Air Pollution Prevention and Control Action Plan*", "*Three-year Plan on Defending the Blue Sky*", and "*Action Plan for continuous improvement of air quality*" to improve air quality (The State Council of the People's Republic of China, 2013, 2018, 2023; Geng et al., 2019). As a result, SO_2 and NO_x concentrations decreased by 59% and 21%, respectively, between 2013-2017 (Zheng et al., 2018). The weighted annual mean $PM_{2.5}$ concentrations also declined from 61.8 to 42.0 μg m^{-3} during this period (Zhang et al., 2019). Similarly, Papachristopoulou et al. (2022) reported a significant negative AOD trends for the Chinese megacities with up to -0.3 per decade during 2003-2020. However, a recent study found that the declining rate of $PM_{2.5}$ concentration has slowed down, from -4.5 μg m^{-3} yr^{-1} in 2013-2017 to -2.3 μg m^{-3} yr^{-1} after 2018; in contrast, the average cost of reducing one unit of $PM_{2.5}$ concentration has risen significantly from 49 billion RMB per μg m^{-3} from 2013-2017 to 100 billion RMB per μg m^{-3} after 2018 (Geng et al., 2024). Similarly, our previous study observed a continuous decline in ground-based lidar-derived tropospheric AOD over Wuhan (30.5°N, 114.4°E) at a rate of -0.049 yr^{-1} from 2010 to 2020 (Yin et al., 2021b). However, the decline in AOD has been less pronounced since 2018, compared to the period from 2010-2017, making it challenging to conclude whether this consistent downward trend in AOD has slowed or even halted at a certain time after 2018. Therefore, it is of great interest to extend the study by involving the subsequent datasets from our polarization lidar observations to well assess the practical long-term variation trends of tropospheric aerosols since 2010. In particular, polarization lidar can distinguish particle backscatter from dust and non-dust aerosol components, making it valuable for analyzing the evolution of natural and anthropogenic aerosol sources (Zhang et al., 2024). This extended analysis would contribute to evaluating the effectiveness of the Chinese government's aerosol emission control policies.

In addition, the vertical distribution of aerosols plays an important role in both global climate and human living environment. The interaction between aerosols and the boundary layer (BL) significantly affects atmospheric stability, while aerosols with extended residence times in the free troposphere (FT) can have more prolonged effects on the climate (Bourgeois et al., 2018). During some air pollution episodes, long-range transported agricultural biomass burning smoke (ABBS) and desert dust are

https://doi.org/10.5194/egusphere-2025-56
Preprint. Discussion started: 10 February 2025

frequently observed in the FT, subsequently interacting with the BL when they deposit (Hänel et al., 2012; Chen et al., 2014; Chen et al., 2017; Lolli et al., 2023). Benefiting from high spatiotemporal resolution, lidar is the most favorable approach for observing aerosol vertical distribution. For instance, during a mega Asian dust event in March 2021, an elevated dust plume was initially detected by ground-based lidar over Wuhan nearly a day before the ground PM_{10} concentration began to rise (He et al., 2022b). Since October 2010, we have conducted routine and consistent lidar observations on the campus of Wuhan University in Wuhan (Yin et al., 2021b; He et al., 2024; Jing et al., 2024), a mega industrial city in central China influenced by local anthropogenic aerosol emissions as well as long-range transported dust and smoke plumes (Lu et al., 2018; Jing et al., 2023). This study serves as a valuable supplement to the long-term evaluation of the optical properties of tropospheric aerosols in China.

This study analyzes the long-term characteristics of tropospheric aerosols over Wuhan from October 2010 to September 2024, based on ground-based polarization lidar observations, together with satellite data, reanalysis data, and surface environment monitoring data. The paper is organized as follows. Section 2 provides a brief description of the instruments and data processing methods employed. Section 3 presents the statistical characteristics of tropospheric aerosols over Wuhan. In Section 4, two typical air pollution events are discussed: one caused by summertime ABBS intrusion and the other by wintertime haze pollution in the low troposphere. In the last section, a summary and conclusions are presented.

2 Instrumentation, data, and methodology

2.1 Polarization lidar in Wuhan

A 532-nm polarization lidar has been routinely operated to observe the vertically resolved optical properties of aerosols over Wuhan (30.5°N, 114.4°E) since October 2010 (Kong and Yi, 2015). Raw lidar data were stored with resolutions of 1 minute and 30 meters. The lowermost height with complete field-of-view (FOV) observation is 0.3 km. The volume (aerosol + molecular) depolarization ratio δ_v (VDR) is calculated as the ratio of perpendicular- to parallel-oriented signals, which can be used to derive the particle depolarization ratio δ_p (PDR) (Freudenthaler et al., 2009). PDR values reflect the non-spherical characteristics of particle shapes, which are in general 0-0.075 for polluted continental/smoke aerosols, 0.075-0.2 for polluted dust, and >0.2 for pure dust (Kim et al., 2018). Note that hygroscopic growth can alter particle shapes, resulting in a decrease in PDR. Fernald method was used to retrieve the total particle backscatter coefficient β_p and particle extinction coefficient α_p, assuming a fixed lidar ratio of 50 sr for the entire statistics, 70 sr for the smoke case, and 57 sr for the urban/industrial aerosol case (Haarig et al., 2018; Zhang et al., 2021a). Moreover, the dust and non-dust backscatter (or extinction) coefficient can be calculated with the method from Tesche et al. (2009). The mass concentration for non-dust component (M_{nd}), which is considered anthropogenic aerosols in this study, are calculated from particle extinction, by multiplying by particle density (1.55 g cm^{-3}), and extinction-to-volume conversion factor (0.44×10^{-12} Mm) (He et al., 2022b). Aerosol optical depth (AOD) is defined as the integral of the particle extinction coefficient for a certain altitude range. In this study, the tropospheric AOD

https://doi.org/10.5194/egusphere-2025-56
Preprint. Discussion started: 10 February 2025

was calculated by integrating α_p values from surface to an altitude of 7 km to ensure a sufficient signal-to-noise ratio (Yin et al., 2021b). Note that α_p values below 0.3 km were assumed equal to that at 0.3 km, possibly causing an uncertainty of <0.05 in AOD (Baars et al., 2017). The uncertainties in the lidar-derived parameters are listed in Table 1. The uncertainty in non-dust extinction is relatively larger due to variability in lidar ratio for continental aerosols, which can be 35 sr for non-absorbing anthropogenic haze and 75 sr for absorbing biomass-burning smoke (Mamouri and Ansmann, 2016).

Table 1. Estimated uncertainties in the lidar-derived parameters.

Parameter	Uncertainty	Reference
Volume depolarization ratio δ_v	<5%	Kong and Yi (2015)
Particle depolarization ratio δ_p	5-10%	Mamouri et al. (2013)
Particle backscatter coefficient β_p	<10%	Zhuang and Yi (2016)
Particle extinction coefficient α_p	<20%	Kafle and Coulter (2013)
Dust backscatter coefficient β_d	10-30%	Mamouri and Ansmann (2016, 2017)
Dust extinction coefficient α_d	15-25%	
Non-dust backscatter coefficient β_{nd}	10-30%	
Non-dust extinction coefficient α_{nd}	20-40%	
Non-dust mass concentration M_{nd}	30-40%	

After cloud screening, cloud-free profiles with a duration time of 30-80 minutes and a vertical resolution of 30 meters are obtained (Yin et al., 2021b). From October 2010 to September 2024, in total 24910 cloud-free profiles were derived from 2307 days for further statistical study (figure 1). Since the installation of a transparent waterproof window in 2017, the lidar system can continuously perform regardless of rainy or snowy conditions, except for occasional maintenance (Yi et al., 2021). Therefore, the number of observation days can even exceed 300 days in recent years (2021-2023).

To improve the representativeness of the long-term statistics, several data quality control policies have been applied in our calculations. Aerosol hygroscopic growth would significantly enhance the observed particle extinction in high humidity conditions (Zieger et al., 2013), which is several times larger than the dry particle extinction. While during severe haze episodes, the particle extinction over Wuhan would not exceed 1.5 km^{-1} according to our previous findings (Zhang et al., 2021). A cloud-free profile having at least one vertical bin with α_p>1.5 km^{-1} was removed to avoid the influence of fog. In total, 676 cloud-free profiles, accounting for 2.7% of the total number of profiles, were removed. Additionally, for representativeness, monthly mean AODs, and extinction coefficients were considered effective only if the number of cloud-free profiles exceeds 15.

https://doi.org/10.5194/egusphere-2025-56
Preprint. Discussion started: 10 February 2025

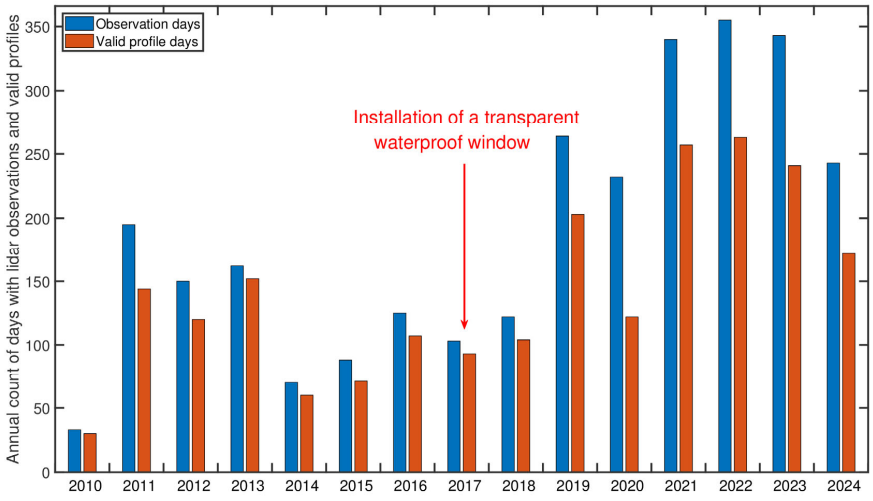

Figure 1. Annual count of days with lidar observations and valid retrievals of aerosol optical parameter profiles (October 2010 to September 2024).

2.2 Satellite data

In addition to ground-based lidar detection, observational data from spaceborne instruments were utilized to depict the horizontal distribution of the aerosol plumes. The Cloud-Aerosol Lidar with Orthogonal Polarization (CALIOP) on board the Cloud-Aerosol Lidar and Infrared Pathfinder Satellite Observation (CALIPSO) launched in 2006 aims to observe the vertically optical properties of cloud and aerosol (Winker et al., 2010). The elastic backscatter and depolarization ratio at 532 nm are measured with vertical and horizontal resolutions of 30 m and 1/3 km below an altitude of 8.2 km. In this study, CALIOP version 4.51 level-1B data products were used to observe the vertical/horizontal distribution and optical properties of a biomass-burning smoke event in June 2014.

The Ozone Mapping and Profiler Suite (OMPS), carried on the Suomi National Polar-orbiting Partnership (Suomi NPP) satellite launched in October 2011 (Jaross et al., 2014), comprises a downward-looking nadir mapper, a nadir profiler, and a limb profiler. Among them, the nadir mapper provides the measurement of UV Aerosol Index (UVAI) with a spatial resolution of 50×50 km, which is an effective indicator of elevated UV-absorbing aerosols (e.g., smoke and dust) (Lee et al., 2015; Tao et al., 2022). In this study, the UVAI provided by OMPS-NPP level 2 data were used to exhibit the spatial evolution of the biomass-burning smoke event in June 2014 near Wuhan.

The Moderate Resolution Imaging Spectroradiometer (MODIS) instrument carried on Terra satellite continually collects data in 36 spectral channels with global coverage every 1-2 days since December 1999. The daily corrected reflectance imagery product is near real-time imagery with a spatial resolution of 0.25 km, which can be used for monitoring wildfires and smoke

https://doi.org/10.5194/egusphere-2025-56
Preprint. Discussion started: 10 February 2025

plumes (Gumley et al., 2010). Moreover, the fire and thermal anomalies provided by MODIS detect the active fire and thermal anomalies with a spatial resolution of 1 km. In this study, the corrected reflectance imageries with the fire and thermal anomalies provided by MODIS on Terra were used to show the source of the biomass-burning smoke event in June 2014.

2.3 HYSPLIT model

The NOAA/ARL (National Oceanic and Atmospheric Administration/Air Resources Laboratory) Hybrid Single Particle Lagrangian Integrated Trajectory (HYSPLIT) model can simulate the forward and backward trajectories of air mass by initializing the starting time, altitude, and geographical location (Draxler and Rolph, 2003; Stein et al., 2015). The meteorological field data from the GDAS archive (Kanamitsu, 1989) were used to drive the mode. In this study, the simulated backward trajectories were used to track the transport pathway of the biomass-burning smoke event in June 2014.

2.4 Air pollution monitoring data

A nationwide air quality monitoring network was established by the Chinese National Environmental Monitoring Center (CNEMC) in 2013, providing an hourly dataset of $PM_{2.5}$, PM_{10}, SO_2, NO_2, CO, and O_3 afterward (Tong et al., 2022). Previous studies show that biomass-burning aerosols and local industrial emissions can strongly increase $PM_{2.5}$, CO, SO_2, and NO_2 concentrations (Ding et al., 2013; Xu et al., 2019; Zhang et al., 2021a). In this study, the $PM_{2.5}$, NO_2, SO_2, and CO concentrations were used to study the long-term variation during 2014-2024 as well as the surface environment in two severe pollution events.

2.5 Radiosonde data

Two radiosondes are usually launched every day around 0000 Universal Time Coordinated (UTC) (0800 local time, LT) and 1200 UTC (2000 LT) ~24 km away from our lidar site. The profiles of pressure, temperature, relative humidity (RH), and other meteorological parameters from the surface to up to ~30 km altitude are measured. The temperature measurement error is <1 °C. The uncertainty in RH is <5% at -10 °C (Nash et al., 2011). In this study, the temperature profiles were used to show the temperature inversion during a haze episode. The RH profiles were used to distinguish haze and fog. The Chinese Meteorological Administration (CMA) defined the haze with the criteria that visibility is <10 km and RH is <80% and the fog-haze mixture with the criteria that visibility is <10 km and RH is 80-95% (China Meteorological Administration, 2019).

2.6 ERA5 reanalysis data

The European Center for Medium-Range Weather Forecasts (ECMWF) reanalysis version 5 (ERA5) is atmospheric reanalysis data of the global climate covering the period from January 1940 onwards, providing the hourly estimates of atmospheric, land, and oceanic climate variables (Hersbach et al., 2020). The boundary layer (BL) height from ERA5 is derived from the ECMWF Integrated Forecasting System's turbulent diffusion and turbulent orographic form drag schemes (Hersbach

https://doi.org/10.5194/egusphere-2025-56
Preprint. Discussion started: 10 February 2025

et al., 2024). In this study, the ERA5 hourly BL height data at 30.5°N and 114.4°E were used to separate non-dust AOD from the BL and FT, respectively, and to show the variation in BL height during two pollution episodes in 2014 and 2019.

3 Long-term evolutions of tropospheric aerosols over Wuhan

3.1 Overview of aerosol optical properties

Figure 2a shows the vertical distribution of the particle extinction coefficient over Wuhan from October 2010 to September 2024. Tropospheric aerosols are mainly concentrated within the boundary layer below 2.0 km, consistent with CALIOP observations in central China (109-116°E and 26-33°N) reported by Lu et al. (2018). Below 1.0 km, severe air pollution with α_p values exceeding 0.6 km^{-1} were more frequent before 2015, suggesting a significant improvement in air quality in recent years. In Figure 2b, the monthly average AODs show a declining trend with a rate of -0.077 yr^{-1} from 2010 to 2017 (here defined as stage I), followed by a fluctuating period from 2018 to 2024 (here defined as stage II). Using MODIS Multi-Angle Implementation of Atmospheric Correction (MAIAC) AOD data, de Leeuw et al., (2022) also found that annual mean AOD stabilized with only a 10% fluctuation around the average across China after 2017, contrasting with the significant decrease in AOD during 2011-2017. Moreover, annual mean AOD over Shanghai (31.0°N, 121.5°E) and Zhengzhou (34.5°N, 113.5°E) also ceased to decline and stabilized at values of 0.4-0.5 after 2018 (de Leeuw et al., 2021).

The significant reduction in AOD during stage I (2010-2017) is mainly attributed to the decrease in three components: local anthropogenic aerosols, regional transboundary smoke, and long-range transported dust. First, the strict policies of anthropogenic emissions control, in particular China's Clean Air Action implemented in 2013, resulted in a substantial reduction in local anthropogenic aerosol emissions. Zhang et al. (2019) reported that the national population-weighted annual mean $PM_{2.5}$ concentrations decreased from 61.8 to 42.0 μg m^{-3} between 2013-2017, attributing to strengthened industrial emission standards, the upgrading of industrial boilers, the phasing out of outdated industrial capacities, and the promoting clean fuels. Second, the widespread enforcement of straw-burning bans during 2013-2018 reduced the long-range transported smoke particles that intruded into Wuhan (Huang et al., 2021). During the harvest season in summer/autumn, large amounts of agricultural biomass burning smoke (ABBS) were generated by the centralized burning of agricultural straws in a short period, resulting in extremely large monthly mean AOD, such as 1.43 in June 2012, and 1.18 in June 2014 (2.7 and 2.3 times compared to grand mean AOD in 2010-2024 with 0.52, in figure 2b). Since the implementation of straw-burning bans, no extreme events with AOD >0.8 have been observed after 2015. Huang et al. (2021) also found a 46.9% reduction in national total $PM_{2.5}$ originating from ABBS during 2013-2018. Third, a decrease in surface wind speed and an increase in vegetation cover over northwestern China led to reduced dust activities in major dust sources, i.e. the Gobi Desert (GD) and Taklimakan Desert (TD), which in turn decreased the dust intrusion into the downstream regions (An et al., 2018). Our previous study also confirmed that the dust optical depth (DOD) in Wuhan showed a decrease rate of -0.011 yr^{-1} from 2010 to 2020 (Jing et al., 2024).

https://doi.org/10.5194/egusphere-2025-56
Preprint. Discussion started: 10 February 2025

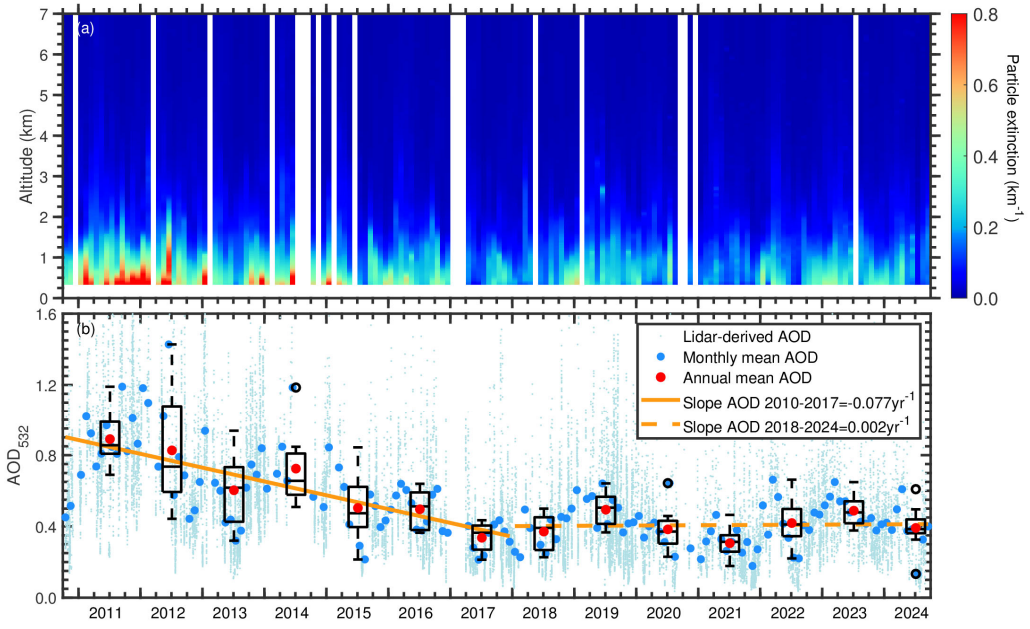

Figure 2. (a) Time-altitude contour plots of the particle extinction coefficient derived from 532-nm polarization lidar observations over Wuhan from 2010 to 2024. White stripes indicate periods with data unavailable due to weather conditions, hardware maintenance, or fewer than 15 cloud-free profiles being recorded in a given month. (b) AOD values for the monthly mean (blue dots) and individual cloud-free profile (light blue dots) over Wuhan during 2010-2024. The orange solid and dashed lines represent the linear fits of the monthly mean AOD for the periods 2010-2017 and 2018-2024, respectively. A box plot is presented for each year during 2011-2024, with the center line indicating the median value and the bottom and top edges representing the 25th and 75th percentiles, respectively. The whiskers are set to be 1.5, and hollow circles denote outliers. Red solid dots represent the annual mean values.

The situation for stage II (2018-2024) differs significantly from stage I. In stage II, AOD generally shows a relatively fluctuating trend. This is because the effectiveness of China's Clean Air Action has decreased after the initial stage of rapid improvement. Geng et al., (2024) found that the average cost of reducing one unit of $PM_{2.5}$ concentration after 2018 (100 billion RMB per $\mu g\,m^{-3}$) was twice that before 2018 (49 billion RMB per $\mu g\,m^{-3}$), resulting in a slower decreasing rate of $PM_{2.5}$ concentration (-2.3 $\mu g\ m^{-3}\ yr^{-1}$ after 2018 versus -4.5 $\mu g\ m^{-3}\ yr^{-1}$ during 2013-2017). Furthermore, aerosol chemistry, i.e., the balance between different pollutants, is another key factor. For example, a decrease in sulfate emissions weakened the ability to neutralize ammonia (NH_3) (Liu et al., 2018), leading to excess NH_3 that forms particulate nitrate, which in turn reduces the effectiveness of control policies (Geng et al., 2024). This may lead to severe air pollution in January 2019 (with a

https://doi.org/10.5194/egusphere-2025-56
Preprint. Discussion started: 10 February 2025

monthly mean AOD of 0.6). In addition, the fluctuations in AOD during stage II can also be attributed to meteorological factors. The annual mean AOD increased from 0.37 to 0.49 during 2018-2019. The precipitation near Wuhan in 2019 decreased by approximately 20-50% compared to the average value of previous years (Zeng et al., 2020), reducing the wet scavenging effect of aerosols (Li et al., 2023). During the winter of 2020-2021, AOD values were relatively low (~0.2-0.3), due to the 'Warm Arctic-Cold Siberia' pattern, which caused cold air from high latitudes to move southward to East China (Zhang et al., 2021b). This led to strong winds and cold waves, aiding the clean of the air. After 2021, the increased monthly mean AOD of 0.46-0.66 in spring was partly due to enhanced dust intrusion from north and northwest China, influenced by an exceptionally strong Mongolian cyclone and surface meteorological anomalies (Gui et al., 2022; Chen et al., 2024).

3.2 Dust variation trend

The mineral dust component primarily represents the aerosols from natural sources (Lu et al., 2018). These dust aerosols mainly originate from major desert regions in East Asia, i.e., the GD and TD, and typically intrude into Wuhan during spring (with a mean DOD of 0.21) and winter (with a mean DOD of 0.15) (Jing et al., 2024). Dust particles are generally blown up by surface wind in the deserts, and then transported southward by cold air and eastward via prevailing westerly. Figure 3 shows the evolution of DOD over Wuhan from 2010 to 2024. Different from the total AOD, which ceased decreasing after 2018, DOD continued to decrease with a rate of -0.011 yr^{-1} until August 2020, as dust emissions are mainly controlled by meteorological factors. The decrease in wind speed and the increase in vegetation cover in northwest China together facilitated the reduction in natural dust emissions prior to 2020 (Xu et al., 2006; An et al., 2018).

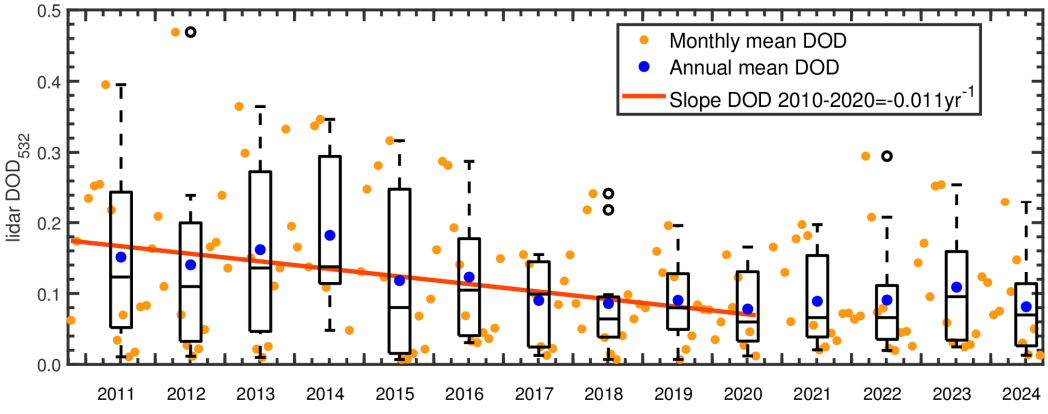

Figure 3. The long-term evolution of DOD for monthly mean (orange dots) from 2010 to 2024. A box plot is presented for each year during 2011-2024, with the blue solid dots representing the annual mean values. Dark orange line represents the linear fit of the monthly mean DOD from 2010 to 2020. The parameters for box plots are the same to figure 2.

https://doi.org/10.5194/egusphere-2025-56
Preprint. Discussion started: 10 February 2025

However, extreme springtime dust events have occurred again in recent years, with average DOD values ranging from 0.16 to 0.20 in spring during 2021-2024, which are larger than spring mean DOD 0.12 in 2020 (the last year of the downward trend). In March 2021, an exceptionally strong Mongolian cyclone, along with a cold high-pressure system developing on the east and west sides of Mongolia, generated a dense pressure gradient and strong surface winds exceeding 20 m s^{-1} over the GD (Gui et al, 2022). Meanwhile, the early spring snowmelt and low soil moisture in the GD provided favorable conditions for dust to be lifted into the atmosphere. He et al., (2022b) reported a severe dust intrusion event over mainland China, with dust concentrations exceeding 100 μg m^{-3} below 2.0 km over Wuhan on 27-30 March 2021. Similar reasons caused the severe dust storm over the GD in the spring of 2023, contributing 77% to the surface dust concentration in southeastern China (Chen et al., 2024, figure 3 therein).

3.3 Anthropogenic aerosol variation trend

In Wuhan, the non-dust component is primarily attributed to anthropogenic aerosols. Figure 4a presents the evolution of non-dust AOD over Wuhan from 2010 to 2024, revealing a trend similar to that of total AOD, i.e., a notable decrease trend with a rate of -0.068 yr-1 (88.3% of the corresponding rate for total AOD) during stage I, followed by a fluctuating period during stage II, characterized by a rate of 0.002 yr-1. This indicates that the reduction in anthropogenic aerosols has been the dominating factor in the significant improvement of Wuhan's local atmospheric environment. We further estimate the respective contributions of anthropogenic aerosols from the boundary layer (BL) and free troposphere (FT). The BL is defined as the strongly turbulent atmospheric layer directly influenced by dynamic, thermal, and other interactions with the Earth's surface (Peng et al., 2023). Aerosols in the BL predominantly originate from local emissions; while, aerosols in the FT are typically from non-local sources via advective transport (Bourgeois et al., 2018). In addition, surface-emitted aerosols can be entrained into the FT through the upward development of convective BL during the daytime. Therefore, partitioning non-dust AOD for the entire atmospheric column into contributions from the BL and FT is conducive to tracing the origins of anthropogenic aerosol from different sources.

Figure 4b shows the evolution of BL and FT non-dust AOD in Wuhan from 2010 to 2024. Over the entire period, the average BL and FT non-dust AOD values are 0.29 and 0.12, respectively, contributing 70.4% and 29.6% to the overall mean non-dust AOD (0.41). In stage I (2010-2017), the BL and FT non-dust AOD decreased at rates of -0.050 yr^{-1} and -0.018 yr^{-1}, respectively, suggesting that the BL non-dust AOD was the primary driver for the total AOD reduction (-0.077 yr^{-1}), contributing 64.9% to the decline. In stage II (2018-2024), both the BL and FT non-dust AODs fluctuate with rates of 0.001 yr^{-1}.

$PM_{2.5}$ has been considered one of the most important air pollutants in BL, with the non-dust components (including organic matter and water-soluble inorganic ions) contributing over 80% in Wuhan (Zhang et al., 2015). To assess air quality in the surface environment of Wuhan, figure 5a shows the evolution of $PM_{2.5}$ concentrations from 2014 to 2024. Similar to the variation of non-dust AODs, the $PM_{2.5}$ concentration decreased sharply with a rate of -7.7 μg m^{-3} yr^{-1} from 2014 to 2017, and then the decline slowed to a rate of -2.6 μg m^{-3} yr^{-1} from 2018 to 2024. This pattern is consistent with the rates of -4.5 μg m^{-3} yr^{-1} from 2013 to 2017 and -2.3 μg m^{-3} yr^{-1} from 2018 to 2020 across China as analyzed by Geng et al. (2024).

https://doi.org/10.5194/egusphere-2025-56
Preprint. Discussion started: 10 February 2025

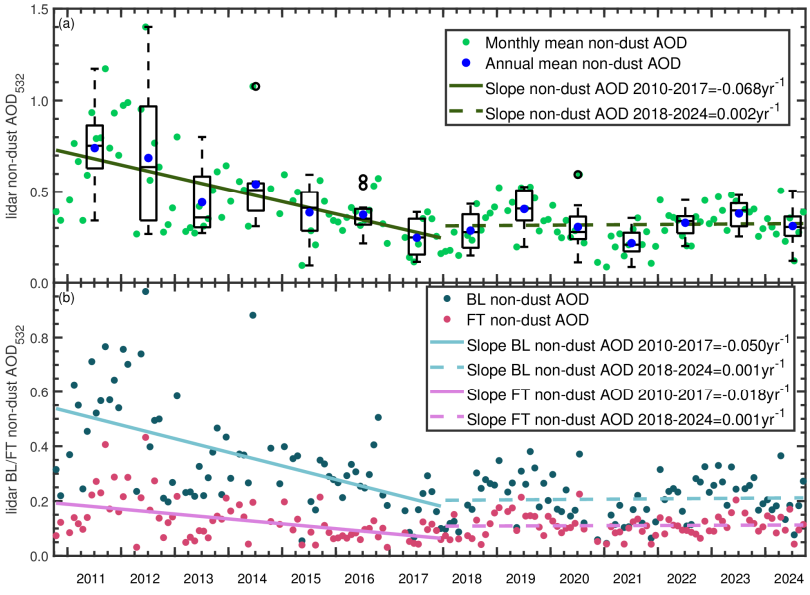

Figure 4. The long-term evolution of (a) non-dust AOD in Wuhan for monthly mean (green dots) from 2010 to 2024. A box plot is presented for each year during 2011-2024, The parameters for box plots are the same to figure 2. Blue solid dots represent the annual mean values. (b) Monthly mean BL (dark green dots) and FT (pink dots) non-dust AOD in Wuhan from 2010 to 2024. Linear fitted lines for the periods 2010-2017 and 2018-2024 are represented by solid and dashed lines, respectively.

To explain the slower decrease in $PM_{2.5}$ concentrations after 2018, figure 5b presents the concentrations of NO_2 and SO_2. These two pollutants can chemically transform into sulfate and nitrate, respectively, which together account for 88.3% of the total water-soluble inorganic ions at an urban site in Wuhan (Zhang et al., 2015). Although SO_2 concentration declined sharply with a rate of -4.5 μg m^{-3} yr^{-1} from 2014 to 2017 due to strengthened industrial emission standards and the upgrading of industrial boilers (Geng et al., 2024), this decline ceased during stage II (after 2018), with a much slower rate of -0.2 μg m^{-3} yr^{-1}. In contrast, NO_2 concentration continued to show a slight downward trend with a rate of -1.4 μg m^{-3} yr^{-1}. The NO_2-to-SO_2 concentration ratio sharply increased from ~ 1.8 in 2014 to ~ 5.3 in 2017, suggesting that NO_2 emissions may have become a more important factor in air pollution during stage II. Liu et al. (2018) found that the rapid reduction in SO_2 emissions would increase the ammonia concentration, leading to the formation of particulate nitrate, which can offset the effectiveness of control. In consequence, the imbalance in emission controls for SO_2 and NO_2 may partly explain the slowed decline in $PM_{2.5}$ concentrations and the fluctuating trend in non-dust AOD during stage II. A severe wintertime haze episode linked to nitrate pollution in Wuhan in January 2019 will be analyzed in detail in Section 4.2.

https://doi.org/10.5194/egusphere-2025-56
Preprint. Discussion started: 10 February 2025

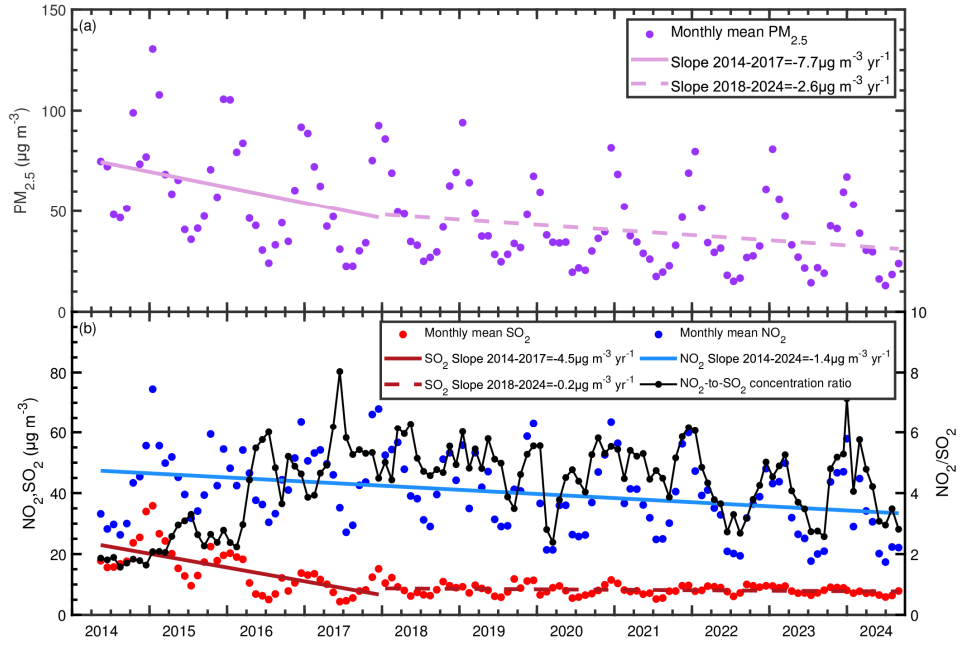

Figure 5. The long-term evolution of monthly mean (a) $PM_{2.5}$ concentration, and (b) SO_2 and NO_2 concentrations from May 2014 to September 2024. Solid and dashed lines represent the linear fits for the periods 2014-2017 and 2018-2024, respectively. The NO_2-to-SO_2 concentration ratio are shown in black.

Figure 6 shows the seasonal average profiles of the non-dust extinction coefficient and monthly variation of BL and FT non-dust AOD from 2010 to 2024. The seasons are defined as spring (March-April-May), summer (June-July-August), autumn (September-October-November), and winter (December-January-February). Approximately 83-88% of anthropogenic aerosols are concentrated below 2 km. The non-dust extinction and mass concentration profiles in summer and autumn are highly consistent, with the largest values observed between 0.7 and 2.5 km with a mean value of 0.12 km^{-1} and approximately 83.0 μg m^{-3}. Additionally, the highest average non-dust AODs in the BL and FT were observed in June (0.36 and 0.16), followed by September (0.35 and 0.14). One of the major reasons was inferred to be the contribution of ABBS from agricultural areas. In China, agricultural straws are intensively combusted during the summer and autumn harvest seasons to enrich cropland nutrients for the next sowing cycle. Based on MODIS fire products, Zha et al. (2013) identified two distinct peaks in agricultural combustion: in June (61-86%) and October (5-14%). Several provinces near Wuhan, including Anhui, Henan, Jiangsu, and Shandong, serve as major agricultural heartlands, accounting for over 80% of agricultural fires. As a result,

https://doi.org/10.5194/egusphere-2025-56
Preprint. Discussion started: 10 February 2025

massive of ABBS are generated from these agricultural areas within a short period, which can rise into the free troposphere and be transported over long distances (Bourgeois et al., 2018). Using CALIOP aerosol subtype classification data, Lu et al. (2018) also found that central China (109°-116°E and 26°-33°N) experiences the highest frequency of smoke at an altitude of 2 km during summer.

It is worth noting that below 0.7 km, the mean α_{nd} and M_{nd} in winter (0.31 km^{-1} and 211.8 μg m^{-3}) are larger than that in summer (0.27 km^{-1} and 185.2 μg m^{-3}) and autumn (0.28 km^{-1} and 193.1 μg m^{-3}). In winter, the high non-dust AODs in the BL were mainly contributed by local anthropogenic aerosols due to the following reasons. First, during winter, low temperatures weaken convective mixing (Miao and Liu, 2019), resulting in a reduced BL height of 0.9 km (yellow dashed line in figure 6a). Low temperatures also facilitate the formation of particulate ammonium nitrate from gaseous ammonia and nitric acid, further increasing NH_4NO_3 concentrations (Han et al., 2008). Second, frequent temperature inversions lead to increased humidity, lower air pressure, and reduced wind speed, which inhibit air circulation and intensify the accumulation of pollutants near the surface (Wu et al., 2014). Third, the concentrations of water-soluble inorganic ions and the relative humidity (71.9%) at the surface are the highest during winter in Wuhan (Zhang et al., 2015), promoting hygroscopic growth, which enhances the particle extinction coefficient and in turn AOD.

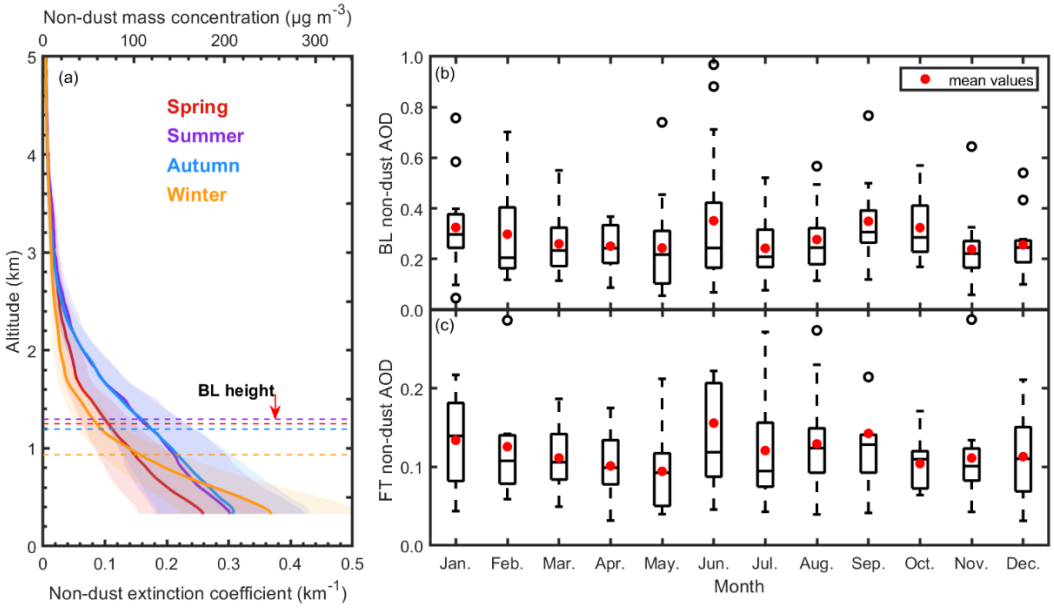

Figure 6. (a) Profiles of seasonal average non-dust extinction coefficient α_{nd} and mass concentration M_{nd}. The seasonal average boundary layer heights are presented by dashed lines. Box plots of the monthly mean (b) BL and (c) FT non-dust AOD for each month from 2010 to 2024. The parameters for box plots are the same to figure 2.

https://doi.org/10.5194/egusphere-2025-56
Preprint. Discussion started: 10 February 2025

4 Case studies on intense pollution episode

As discussed in Section 3, massive amounts of ABBS are generated from agricultural straws during the summer harvest season, which can be transported over a long distance to Wuhan, resulting in pronounced extinction features at FT and BL in summer. In addition, the increased contribution of nitrate pollution near the surface in winter after 2018 may partially offset the pollution control efforts during stage II. Here, two typical air pollution cases are presented: summertime transboundary ABBS in June 2014 and wintertime local anthropogenic aerosol pollution in January 2019.

4.1 Summertime biomass burning smoke case in June 2014

A notable agricultural straw combustion event occurred on 9-13 June 2014, as seen in Figure 7, which includes multi-spaceborne observations (MODIS, OMPS, and CALIOP) over the region spanning 29-35°N and 112-118°E. Most fire hotspots were concentrated in northern Anhui province, generating distinct smoke plumes (gray areas). The daily evolution of UVAI (figures 7f-j) shows that the ABBS plumes initially formed in Henan and Anhui Province and were subsequently transported southwestward toward Wuhan and the surrounding regions during this period. On 10 June, the CALIOP-observed total attenuated backscatter and volume depolarization ratio indicated that the ABBS plumes were mainly distributed from the surface to an altitude of 5 km, with a slightly enhanced volume depolarization ratio of 0-0.1.

Figure 8a shows the hourly surface $PM_{2.5}$ and CO concentrations in Wuhan during June 2014, together with the OMPS-measured UVAI between 0400 and 0600 LT during 9-13 June. On 9 June, the UVAI value was nearly zero, indicating the presence of UV-absorbing aerosols and confirming that the fresh smoke particles had not yet arrived. By 13 June, with the arrival of ABBS, the $PM_{2.5}$ and CO concentrations, as well as UVAI values sharply increased to 479.0 μg m^{-3}, 2.1 mg m^{-3}, and 4.2, respectively, revealing the presence of massive smoke particles. Lidar observations in Wuhan during the period marked by the green shading in Figure 8a are presented in Figures 8b-k. It should be noted that the lidar system did not operate before 1600 LT on 10 June and after 0400 LT on 12 June. During these three days, the major aerosol layer consistently appeared below altitudes of 3-4 km, with δ_v values below 0.1 and AODs ranging from 1.35 to 2.16. A three-day backward trajectory of air masses originating from Wuhan at 2000 LT on 11 June passed through the fire sites (figure 7a), further confirming that the observed aerosols were ABBS. Severe air pollution was observed below 1.0 km with a mean α_p of 0.85-1.31 km^{-1}, which was associated with low BL height (<1.5 km) and temperature inversion (at 0.2-0.5 km and 1.2-1.4 km). Absorptive aerosols (e.g. black carbon (BC) from biomass burning) can heat the BL and depress the height of BL (Ding et al., 2016). Additionally, the mean δ_p of 0.06-0.07 and 0.08-0.11 were derived below and above 1.0 km, respectively, indicating that the mix between smoke and urban/industrial pollutants under higher RH conditions would promote the hygroscopic growth, leading to the enhanced α_p and decreased δ_p (Miri et al., 2024). Therefore, the calculation of mass concentration is prone to significant errors and is not presented here.

https://doi.org/10.5194/egusphere-2025-56
Preprint. Discussion started: 10 February 2025

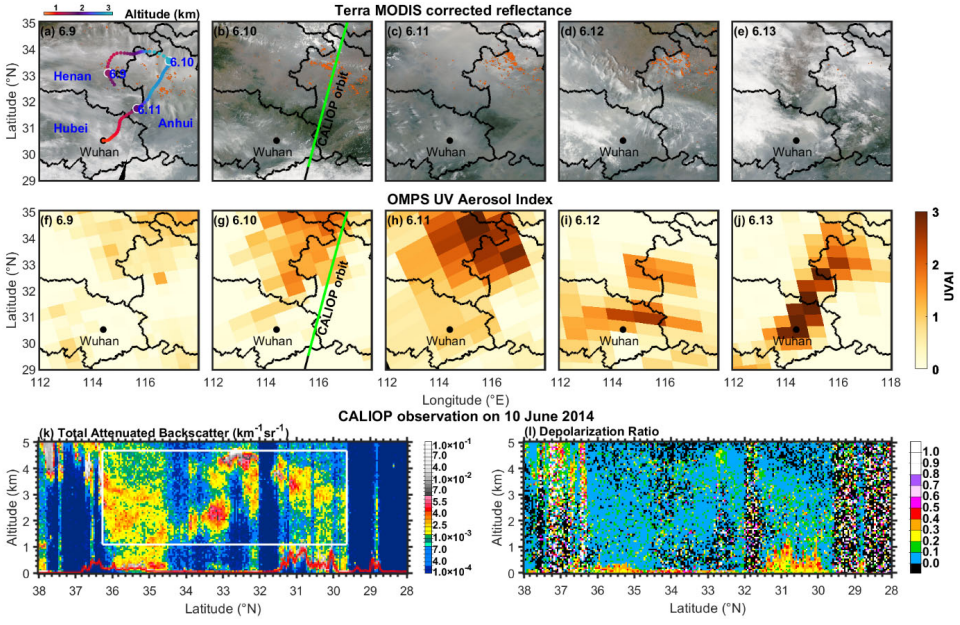

Figure 7. (a-e) MODIS corrected reflectance and fire/thermal anomalies near Wuhan from 9-13 June (MODIS, 2024). Panel (a) includes a 3-d backward trajectory originating from Wuhan at 2000 LT at an altitude of 0.8 km; (f-j) UVAI measurements from OMPS during 8-13 June; CALIOP-observed 532-nm (k) total attenuated backscatter coefficient and (l) volume depolarization ratio on 10 June. The CALIOP orbit footprints corresponding to (k) and (l) are shown in (b) and (g), with green lines highlighting the presence of smoke plumes.

Zhang et al. (2014) reported a severe air pollution event near Wuhan in June 2012, caused by ABBS originating from Anhui Province. This event led to an increased $PM_{2.5}$ concentration by nearly an order of magnitude and BC concentration by more than 3 times, compared to normal conditions. The aerosol layers were primarily observed below 1 km, with average particle extinction coefficients as high as 1 km^{-1} according to CALIOP observations, which were comparable to those of 0.85-1.31 km^{-1} observed in the case presented in this study. On 3 June 2011, another intense ABBS episode occurred in Nanjing (31.5°N, 118.5°E), resulting in an increased AODs of 0.6-3.0 at 500 nm (Wu et al., 2017). Ground-based lidar observations revealed that the major aerosol layers were located below 1.5 km, with significantly enhanced extinction coefficients exceeding 1.0 km^{-1}. In general, ABBS from agricultural straw combustion during summer were a common phenomenon in the past decades and caused frequent severe air pollution. However, this is no longer the case according to our long-term lidar monitoring in recent years. This shift can be attributed to the several enforcements of straw burning bans (Huang et al., 2021; Wang et al., 2023), incentive programs to encourage a comprehensive use of straws, and the development of biomass energy (Sun et al., 2019).

https://doi.org/10.5194/egusphere-2025-56
Preprint. Discussion started: 10 February 2025

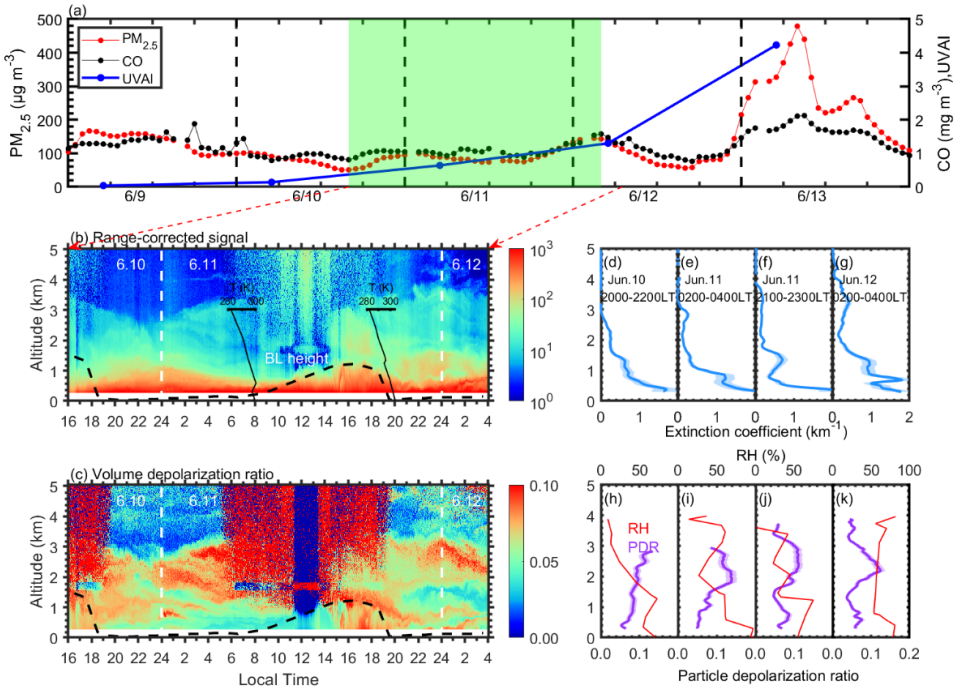

Figure 8. (a) $PM_{2.5}$, CO concentrations at the surface, and UVAI measured by OMPS in Wuhan on 9-13 June 2014. Time-altitude contour plots of (b) range-corrected signal and (c) volume depolarization ratio measured by polarization lidar over Wuhan from 10 to 12 June (local time, UTC+8). The green shaded area indicates the period of lidar observations. The Black dashed line denotes the BL height, while black solid lines represent temperature profiles measured by radiosondes at around 0800 and 2000 LT on 11 June. Selected typical profiles of (d-g) extinction coefficient and (h-k) particle depolarization ratio. Relative humidity profiles at 0800 LT (0000 UTC) from 10-12 June are shown in panels (h-k).

4.2 Wintertime haze case in January 2019

A severe haze episode in January 2019, as shown in Figure 9. On 23-25 January, two peaks of NO_2 concentration with 120-125 μg m^{-3} and three peaks of O_3 concentration with 85-100 μg m^{-3} were measured, which were the main gaseous precursors of nitrate (Xu et al. 2019). Subsequently, on 25 January, the $PM_{2.5}$ concentration approximately doubled from 94 μg m^{-3} at noon up to 185 μg m^{-3} at night. It can be inferred that the increase in $PM_{2.5}$ concentration on 25 January was mainly contributed by nitrate formed by large emissions of NO_2 and O_3 in the past two days. The water-soluble inorganic ions, especially nitrate, are the majority components of $PM_{2.5}$, which generally cause severe haze episodes in winter (Zhang et al., 2015).

https://doi.org/10.5194/egusphere-2025-56
Preprint. Discussion started: 10 February 2025

Figures 9b-k show the corresponding lidar observations during 23-26 January. Aerosols were predominantly concentrated below 1.5 km throughout the four days. Consistent with the increase in $PM_{2.5}$ concentrations on 25 January, the AOD increased approximately 6.1 times, from 0.20 to 1.22, over the period from 23-26 January. It is noted that the increase in AOD was more pronounced than that in $PM_{2.5}$ levels. Previous studies have shown that an increase in nitrate fractions facilitates the particle hygroscopic growth (Wang et al., 2020; Hu et al., 2021b), leading to higher α_p and lower δ_p (Zieger et al., 2013; Tan et al., 2019). Accordingly, on 26 January, a larger mean α_p of 1.11 km^{-1} and a lower mean δ_p of 0.05 were derived below 1.0 km, compared to values of 0.17-0.19 km^{-1} and 0.11 on 23-24 January, respectively. This suggests a shift in the dominant aerosol type near the surface, from a non-spherical dust and urban aerosol mixture on 23-24 January to hygroscopic and spherical nitrate particles by 26 January. For comparison, a similar haze episode in Wuhan in January 2013, reported by Zhang et al. (2021a), exhibited comparable characteristics, including a low δ_p of 0.05 (at 532 nm) and a high AOD of 1.32 (at 500 nm).

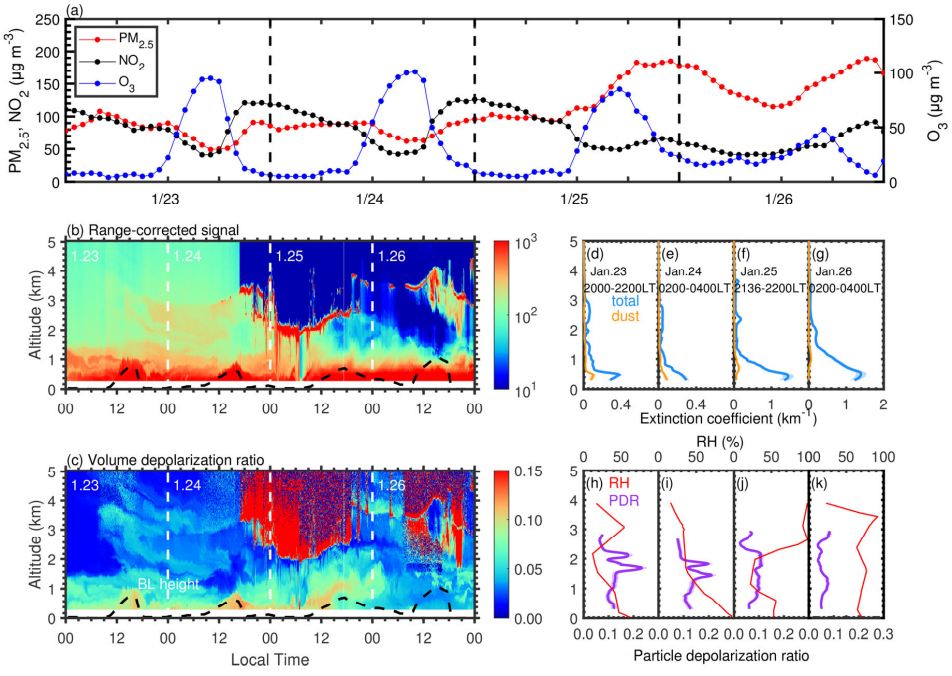

Figure 9. (a) Concentrations of $PM_{2.5}$, NO_2, and O_3 in Wuhan on 23-26 January 2019, and time-altitude contour plots of (b) range-corrected signal and (c) volume depolarization ratio measured by polarization lidar over Wuhan during the same period. The black dashed line represents the BL height. Selected typical profiles of (d-g) extinction coefficient and (h-k) particle depolarization ratio. Relative humidity profiles at 0800 LT (0000 UTC) from 23-26 January are shown in panels (h-k).

https://doi.org/10.5194/egusphere-2025-56
Preprint. Discussion started: 10 February 2025

5 Summary and conclusions

This study examines the long-term characteristics of tropospheric aerosols over Wuhan from 2010 to 2024, using ground-based polarization lidar observations together with surface pollution monitoring data, ERA5 reanalysis data, radiosonde measurements, and multi-satellite observations. The long-term variation in total AOD can be divided into two phases: a declining trend with a rate of -0.077 yr^{-1} during 2010-2017 (stage I) and a fluctuating period during 2018-2024 (stage II). Similarly, the surface $PM_{2.5}$ concentration decreased rapidly with a rate of -7.7 μg m^{-3} yr^{-1} during stage I, followed by a slower reduction of -2.6 μg m^{-3} yr^{-1} during stage II. These long-term trends in AOD and $PM_{2.5}$ concentrations are consistent with findings from previous studies covering similar periods (de Leeuw et al., 2021, 2022; Geng et al., 2024).

The contribution of AOD was further divided into natural (dust) and anthropogenic (non-dust) aerosol components. For the dust component, the DOD consistently decreased with a rate of -0.011 yr^{-1} until August 2020, attributed to reduced surface wind speeds in Asian dust source regions and increased vegetation cover in northwestern China, both of which mitigated the long-range transport of dust aerosols to Wuhan (Jing et al., 2024). However, it is noteworthy that extreme Asian dust storm outbreaks have become more frequent and intense during spring in the past four years (since 2021), due to the exceptionally strong Mongolian cyclone condition, early spring snowmelt, and low soil moisture in the GD (Gui et al, 2022).

For the anthropogenic aerosol (non-dust) component, its AOD in general exhibited a trend similar to that of total AOD. During stage I, the non-dust AOD contributed 88.3% to the reduction in total AOD (-0.068 yr^{-1} versus -0.077 yr^{-1}). This reduction was primarily contributed by the decrease in BL AOD (contributing 64.9% to total AOD), highlighting the significant impact of reduced emissions of local anthropogenic aerosols due to effective government policies. During stage II, the non-dust AOD fluctuated with a rate of 0.002 yr^{-1}. The imbalanced control of SO_2 and NO_2 emissions led to a sharp rise in the NO_2-to-SO_2 concentration ratio, from approximately 1.8 in 2014 to 5.3 in 2017, which may have partially offset the pollution control efforts during stage II. The seasonal characteristics of anthropogenic aerosols were also analyzed. In summer and autumn, anthropogenic aerosols showed enhanced extinction coefficient (0.12 km^{-1}) and mass concentration (83.0 μg m^{-3}) at altitudes of 0.7-2.5 km, mainly due to smoke produced by agricultural-straw combustion. In contrast, anthropogenic aerosols in winter were generally concentrated below 0.7 km, with much higher α_{nd} and M_{nd} of 0.31 km^{-1} and 211.8 μg m^{-3}, respectively.

In addition, two typical air pollution case studies were presented: summertime transboundary ABBS in June 2014 and wintertime local anthropogenic aerosol pollution in January 2019. From 9-13 June 2014, ABBS plumes originating from agricultural straw combustion in Anhui Province were transported to Wuhan. The smoke layer was generally located below 4 km, with AOD values of 1.35-2.16. Within the BL, plenty of aerosols were observed below 1 km, with α_p values of 0.85-1.31 km^{-1} and δ_p values of 0.06-0.07, suggesting the predominance of aged smoke particles. In January 2019, a severe haze event occurred in Wuhan, with $PM_{2.5}$ concentrations reaching up to 185 μg m^{-3} on 25 January. Meanwhile, the AOD increased 6.1 times, from 0.20 on 23 January to 1.22 on 26 January. On 26 January, a significant large α_p of 1.11 km^{-1} and relatively low δ_p of 0.05 were recorded below 1 km, suggesting the accumulation of spherical anthropogenic aerosols.

https://doi.org/10.5194/egusphere-2025-56
Preprint. Discussion started: 10 February 2025

Our previous work (Yin et al., 2021b) took advantage of polarization lidar observations to examine the long-term variation in the optical properties of tropospheric aerosols over Wuhan from 2010 to 2020, revealing a downward trend in tropospheric AOD. The present study, as an extension of Yin et al. (2021b), updates the observational results to include the most recent four years and reports a halt in the reduction of AOD since 2018. This updated analysis promotes our understanding of how Wuhan's atmospheric environment responds to the government's anthropogenic emission control policies and natural mineral dust activities in East Asian desert regions. Due to the limitations of single-wavelength polarization lidar, distinguishing smoke aerosols from locally emitted urban aerosols is only feasible by incorporating large-scale spaceborne observations and simulations of air mass backward trajectories. In the future, we plan to involve observations from pure rotational Raman lidars at both 355 nm and 532 nm (Pan et al., 2020; Liu et al., 2019; Yi et al., 2024). This will enable the exploration of the relationship between lidar ratio and particle depolarization ratio (Peng et al., 2021; Floutsi et al., 2023), facilitating the classification of aerosol types. In addition, the particle extinction coefficient is known to increase significantly due to the hygroscopic growth of aerosols under high humidity conditions (Zieger et al., 2013). This phenomenon will be analyzed in future studies to further evaluate the long-term variation in the dry optical properties of tropospheric aerosols over Wuhan.

Data availability

CALIOP data can be obtained from https://subset.larc.nasa.gov/ (CALIPSO, 2025). OMPS data can be obtained from https://www.earthdata.nasa.gov/sensors/omps (OMPS, 2025). MODIS daily corrected reflectance imageries can be obtained from https://worldview.earthdata.nasa.gov/ (MODIS, 2025). ERA5 reanalysis data can be obtained from https://cds.climate.copernicus.eu/datasets (ERA5, 2025). The air pollution monitoring data can be obtained from http://www.cnemc.cn. The radiosonde data can be obtained from http://weather.uwyo.edu/upperair/sounding.html. The HYSPLIT model is available at https://www.arl.noaa.gov (HYSPLIT, 2025). Lidar data used to generate the results of this paper are available from the authors upon request (e-mail: yf@whu.edu.cn).

Author contributions

YH, DJ, and ZY analyzed the data and wrote the manuscript. ZY, KH and FL participated in scientific discussions and reviewed and proofread the manuscript. YH and FY conceived the research and acquired the research funding. FY led the study.

Competing interests

The contact author has declared that none of the authors has any competing interests.

https://doi.org/10.5194/egusphere-2025-56
Preprint. Discussion started: 10 February 2025

Financial support

This work was supported by the National Natural Science Foundation of China (grant nos. 42005101, 41927804, and 42205130), the Hubei Provincial Natural Science Foundation of China (2023AFB617), and the Meridian Space Weather Monitoring Project (China).

Acknowledgements

The authors thank the colleagues who participated in the operation of the lidar system at our site. We also acknowledge the Atmospheric Science Data Central (ASDC) at the National Aeronautics and Space Administration (NASA) Langley Research Center for providing the CALIPSO data, NASA/National Oceanic and Atmospheric Administration (NOAA) for the OMPS data, NASA Earth Science Data and Information System (ESDIS) project for MODIS daily corrected reflectance imageries, the European Centre for Medium-Range Weather Forecasts (ECMWF) for ERA5 reanalysis data, the China National Environmental Monitoring Center (CNEMC) for Air pollution monitoring data, the University of Wyoming for radiosonde data, and the NOAA Air Resources Laboratory (ARL) for the HYSPLIT model.

References

An, L., Che, H., Xue, M., Zhang, T., Wang, H., Wang, Y., Zhou, C., Zhao, H., Gui, K., Zheng, Y., Sun, T., Liang, Y., Sun, E., Zhang, H., and Zhang, X.: Temporal and spatial variations in sand and dust storm events in East Asia from 2007 to 2016: Relationships with surface conditions and climate change, Sci. Total Environ., 633, 452–462. https://doi.org/10.1016/j.scitotenv.2018.03.068, 2018.

Ansmann, A., Mamouri, R.E., Hofer, J., Baars, H., Althausen, D., and Abdullaev, S.F.: Dust mass, cloud condensation nuclei, and ice-nucleating particle profiling with polarization lidar: updated POLIPHON conversion factors from global AERONET analysis, Atmos. Meas. Tech., 12, 4849–4865, https://doi.org/10.5194/amt-12-4849-2019, 2019.

Baars, H., Seifert, P., Engelmann, R., and Wandinger, U.: Target categorization of aerosol and clouds by continuous multiwavelength-polarization lidar measurements, Atmos. Meas. Tech., 10, 3175–3201, https://doi.org/10.5194/amt-10-3175-2017, 2017.

Bellouin, N., Quaas, J., Gryspeerdt, E., Kinne, S., Stier, P., Watson-Parris, D., Boucher, O., Carslaw, K.S., Christensen, M., Daniau, A.-L., Dufresne, J.-L., and Feingold, G.: Bounding global aerosol radiative forcing of climate change, Rev. Geophys., 58, e2019RG000660, https://doi.org/10.1029/2019RG000660, 2019.

Bourgeois, Q., Ekman, A. M. L., Renard, J.-B., Krejci, R., Devasthale, A., Bender, F. A.-M., Riipinen, I., Berthet, G., and Tackett, J. L.: How much of the global aerosol optical depth is found in the boundary layer and free troposphere?, Atmos. Chem. Phys., 18, 7709–7720, https://doi.org/10.5194/acp-18-7709-2018, 2018.

https://doi.org/10.5194/egusphere-2025-56
Preprint. Discussion started: 10 February 2025

CALIPSO: Cloud-Aerosol Lidar and Infared Pathfinder Satellite Observation data base, EarthData [data set], https://subset.larc.nasa.gov/ (last access: 20 November 2024), 2025

Chen, J., Li, C., Ristovski, Z., Milic, A., Gu, Y., Islam, M. S., Wang, S., Hao, J., Zhang, H., He, C., Guo, H., Fu, H., Miljevic, B., Morawska, L., Thai, P., Lam, Y. F., Pereira, G., Ding, A., Huang, X., and Dumka, U. C.: A review of biomass burning: Emissions and impacts on air quality, health and climate in China, Sci. Total Environ., 579, 1000–1034, https://doi.org/10.1016/j.scitotenv.2016.11.025, 2017.

Chen, Y., Chen, S., Bi, H., Zhou, J., and Zhang, Y.: Where is the Dust Source of 2023 Several Severe Dust Events in China?, Bull. Amer. Meteor. Soc., 105, E2085–E2096, https://doi.org/10.1175/BAMS-D-23-0121.1, 2024.

Chen, Z.Y., Liu, W.Q., Heese, B., Althausen, D., Baars, H., Cheng, T.H., Shu, X.W., and Zhang, T.S.: Aerosol optical properties observed by combined Raman-elastic backscatter lidar in winter 2009 in Pearl River Delta, South China, J. Geophys. Res.-Atmos., 119, 2496–2510, https://doi.org/10.1002/2013JD020200, 2014.

China Meteorological Administration: Haze identification for meteorological observation, available at: https://www.cma.gov.cn/zfxxgk/gknr/flfgbz/bz/202009/t20200922_2137575.html (last access: 2 January 2025), 2019 (in Chinese).

Cohen, A. J., Brauer, M., Burnett, R., Anderson, H. R., Frostad, J., Estep, K., Balakrishnan, K., Brunekreef, B., Dandona, L., and Dandona, R.: Estimates and 25-year trends of the global burden of disease attributable to ambient air pollution: an analysis of data from the Global Burden of Diseases Study 2015, Lancet, 389, 1907–1918, 2017.

Copernicus Climate Change Service, Climate Data Store: ERA5 hourly data on single levels from 1940 to present. Copernicus Climate Change Service (C3S) Climate Data Store (CDS), [data set], https://doi.org/10.24381/cds.adbb2d47 (last access: 21 November 2024), 2025.

de Leeuw, G., van der A, R., Bai, J., Xue, Y., Varotsos, C., Li, Z., Fan, C., Chen, X., Christodoulakis, I., Ding, J., Hou, X., Kouremadas, G., Li, D., Wang, J., Zara, M., Zhang, K., and Zhang, Y.: Air Quality over China, Remote Sens., 13, 3542, https://doi.org/10.3390/rs13173542, 2021.

de Leeuw, G., Fan, C., Li, Z., Dong, J., Li, Y., Ou, Y., and Zhu, S.: Spatiotemporal variation and provincial scale differences of the AOD across China during 2000–2021, Atmos. Pollut. Res., 13, 101359, https://doi.org/10.1016/j.apr.2022.101359, 2022.

Ding, A, Huang, X., Nie, W., Sun, J., Kerminen, V.-M., Petäjä, T., Su, H., Cheng, Y., Yang, X., Wang, M., Chi, X., Wang, J., Virkkula, A., Guo, W., Yuan, J., Wang, S., Zhang, R., Wu, Y., Song, Y., Zhu, T., Zilitinkevich, S., Kulmala, M., and Fu, C.: Enhanced haze pollution by black carbon in megacities in China, Geophys. Res. Lett., 43, 2873–2879, https://doi.org/10.1002/2016GL067745, 2016.

Draxler, R. and Rolph, G.: HYSPLIT (Hybrid Single-Particle Lagrangian Integrated Trajectory) Model, Air Resources Laboratory, NOAA, Silver Spring, Md, USA, https://www.ready.noaa.gov/HYSPLIT.php (last access: 10 November 2024), 2003.

https://doi.org/10.5194/egusphere-2025-56
Preprint. Discussion started: 10 February 2025

Floutsi, A. A., Baars, H., Engelmann, R., Althausen, D., Ansmann, A., Bohlmann, S., Heese, B., Hofer, J., Kanitz, T., Haarig, M., Ohneiser, K., Radenz, M., Seifert, P., Skupin, A., Yin, Z., Abdullaev, S. F., Komppula, M., Filioglou, M., Giannakaki, E., Stachlewska, I. S., Janicka, L., Bortoli, D., Marinou, E., Amiridis, V., Gialitaki, A., Mamouri, R.-E., Barja, B., and Wandinger, U.: DeLiAn – a growing collection of depolarization ratio, lidar ratio and Ångström exponent for different aerosol types and mixtures from ground-based lidar observations, Atmos. Meas. Tech., 16, 2353–2379, https://doi.org/10.5194/amt-16-2353-2023, 2023.

Freudenthaler, V., Esselborn, M., Wiegner, M., Heese, B., Tesche, M., Ansmann, A., Müller, D., Althausen, D., Wirth, M., Fix, A., Ehret, G., Knippertz, P., Toledano, C., Gasteiger, J., Garhammer, M., and Seefeldner, M.: Depolarization ratio profiling at several wavelengths in pure Saharan dust during SAMUM2006, Tellus B, 61, 165–179, https://doi.org/10.1111/j.1600-0889.2008.00396.x, 2009.

Geng, G., Xiao, Q., Zheng, Y., Tong, D., Zhang, Y., Zhang, X., Zhang, Q., He, K., and Liu, Y.: Impact of China's air pollution prevention and control action plan on $PM_{2.5}$ chemical composition over eastern China, Sci. China Earth Sci., 62, 1872–1884, https://doi.org/10.1007/s11430-018-9353-x, 2019.

Geng, G., Liu, Y., Liu, Y., Liu, S., Cheng, J., Yan, L., Wu, N., Hu, H., Tong, D., Zheng, B., Yin, Z., He, K., and Zhang, Q.: Efficacy of China's clean air actions to tackle $PM_{2.5}$ pollution between 2013 and 2020, Nat. Geosci., 17, 987–994, https://doi.org/10.1038/s41561-024-01540-z, 2024.

Gui, K., Yao, W., Che, H., An, L., Zheng, Y., Li, L., Zhao, H., Zhang, L., Zhong, J., Wang, Y., and Zhang, X.: Record-breaking dust loading during two mega dust storm events over northern China in March 2021: aerosol optical and radiative properties and meteorological drivers, Atmos. Chem. Phys., 22, 7905–7932, https://doi.org/10.5194/acp-22-7905-2022, 2022.

Gumley, L., Descloitres, J., and Schmaltz, J.: Creating Reprojected True Color MODIS Images: A Tutorial, Version 1.0.2, University of Wisconsin-Madison and NASA Goddard Space Flight Center, available at: https://cdn.earthdata.nasa.gov/conduit/upload/946/MODIS_True_Color.pdf (last access: 20 November 2024), 17 pp., 2010.

Haarig, M., Ansmann, A., Baars, H., Jimenez, C., Veselovskii, I., Engelmann, R., and Althausen, D.: Depolarization and lidar ratios at 355, 532, and 1064 nm and microphysical properties of aged tropospheric and stratospheric Canadian wildfire smoke, Atmos. Chem. Phys., 18, 11847–11861, https://doi.org/10.5194/acp-18-11847-2018, 2018.

Han, Y., Kim, T., Kim, H.: Ionic constituents and source analysis of $PM_{2.5}$ in three Korean cities, Atmos. Environ., 42, 4735–4746, https://doi.org/10.1016/j.atmosenv.2008.01.047. 2008.

Hänel, A., Baars, H., Althausen, D., Ansmann, A., Engelmann, R., and Sun, J.Y.: One year aerosol profiling with EUCAARI Raman lidar at Shangdianzi GAW station: Beijing plume and seasonal variations, J. Geophys. Res.-Atmos., 117, 1–11, https://doi.org/10.1029/2012JD017577, 2012.

https://doi.org/10.5194/egusphere-2025-56
Preprint. Discussion started: 10 February 2025

He, Y., Yi, F., Yi, Y., Liu, F., and Zhang, Y.: Heterogeneous nucleation of midlevel cloud layer influenced by transported Asian dust over Wuhan (30.5◦N, 114.4◦E), China, J. Geophys. Res.-Atmos., 126, e2020JD033394, https://doi.org/10.1029/2020JD033394, 2021.

He, Y., Yi, F., Liu, F., Yin, Z., and Zhou, J.: Ice nucleation of cirrus clouds related to the transported dust layer observed by ground-based lidars over Wuhan, China. Adv. Atmos. Sci. 39, 2071–2086. https://doi.org/10.1007/s00376-021-1192-x, 2022a.

He, Y., Yi, F., Yin, Z., Liu, F., Yi, Y., and Zhou, J.: Mega Asian dust event over China on 27–31 March 2021 observed with space-borne instruments and ground-based polarization lidar, Atmos. Environ., 285, 119238 https://doi.org/10.1016/j.atmosenv.2022.119238, 2022b.

He, Y., Jing, D., Yin, Z., Ohneiser, K., and Yi, F.: Long-term (2010–2021) lidar observations of stratospheric aerosols in Wuhan, China, Atmos. Chem. Phys., 24, 11431–11450, https://doi.org/10.5194/acp-24-11431-2024, 2024.

Hersbach, H., Bell, B., Berrisford, P., Hirahara, S., Hor´anyi, A., Munoz-Sabater,˜ J., Nicolas, J., Peubey, C., Radu, R., Schepers, D., Simmons, A., Soci, C., Abdalla, S., Abellan, X., Balsamo, G., Bechtold, P., Biavati, G., Bidlot, J., Bonavita, M., De Chiara, G., Dahlgren, P., Dee, D., Diamantakis, M., Dragani, R., Flemming, J., Forbes, R., Fuentes, M., Geer, A., Haimberger, L., Healy, S., Hogan, R.J., Holm,´ E., Janiskova,´ M., Keeley, S., Laloyaux, P., Lopez, P., Lupu, C., Radnoti, G., de Rosnay, P., Rozum, I., Vamborg, F., Villaume, S., and Thépaut, J.-N.: The ERA5 global reanalysis, Q. J. Roy. Meteor. Soc., 146, 1999–2049. https://doi.org/10.1002/qj.3803, 2020.

Hersbach, H., Bell, B., Berrisford, P., Biavati, G., Horányi, A., Muñoz Sabater, J., Nicolas, J., Peubey, C., Radu, R., Rozum, I., Schepers, D., Simmons, A., Soci, C., Dee, D., and Thépaut, J.-N.: ERA5 hourly data on single levels from 1940 to present. Copernicus Climate Change Service (C3S) Climate Data Store (CDS), https://doi.org/10.24381/cds.adbb2d47, last access: 10 November 2024.

Hu, Z., Jin, Q., Ma, Y., Pu, B., Ji, Z., Wang, Y., and Dong, W.: Temporal evolution of aerosols and their extreme events in polluted Asian regions during Terra's 20-year observations, Remote Sens. Environ., 263, 112541, https://doi.org/10.1016/j.rse.2021.112541, 2021a.

Hu, S., Zhao, G., Tan, T., Li, C., Zong, T., Xu, N., Zhu, W., Hu, M.: Current challenges of improving visibility due to increasing nitrate fraction in PM2. 5 during the haze days in Beijing, China, Environ. Pollut., 290, 118032, https://doi.org/10.1016/j.envpol.2021.118032, 2021b.

Huang, J., Wang, T., Wang, W., Li, Z., Yan, H.: Climate effects of dust aerosols over East Asian arid and semiarid regions, J. Geophys. Res.-Atmos., 119, 11,398–11,416, https://doi.org/10.1002/2014JD021796, 2014.

Huang L, Zhu Y, Wang Q, Zhu A, Liu Z, Wang Y, Allen, D. T., and Li, L: Assessment of the effects of straw burning bans in China: emissions, air quality, and health impacts, Sci. Total Environ., 789, 147935, https://doi.org/10.1016/j.scitotenv.2021.147935, 2021.

HYSPLIT: Hybrid Single Particle Lagrangian Integrated Trajectory, NOAA [data set], https://www.arl.noaa.gov/ (last access: 11 November 2024), 2025.

https://doi.org/10.5194/egusphere-2025-56
Preprint. Discussion started: 10 February 2025

IPCC, 2021. Climate change 2021: the physical science basis. In: Masson-Delmotte, V., Zhai, P., Pirani, A., Connors, S.L., P´ean, C., Berger, S., Caud, N., Chen, Y., Goldfarb, L., Gomis, M.I., Huang, M., Leitzell, K., Lonnoy, E., Matthews, J.B.R., Maycock, T.K., Waterfield, T., Yelekçi, O., Yu, R., Zhou, B. (Eds.), Contribution of Working Group I to the Sixth Assessment Report of the Intergovernmental Panel on Climate Change. Cambridge University Press, Cambridge, United Kingdom and New York, NY, USA.

Jaross, G., Bhartia, P. K., Chen, G., Kowitt, M., Haken, M., Chen, Z., Xu P., Warner, J., and Kelly, T.: OMPS Limb Profiler instrument performance assessment, J. Geophys. Res.-Atmos., 119, 4399–4412, https://doi.org/10.1002/2013JD020482, 2014.

Jing, D., He, Y., Yin, Z., Liu, F., and Yi, F.: Long-term characteristics of dust aerosols over central China from 2010 to 2020 observed with polarization lidar. Atmos. Res., 297, 107129, https://doi.org/10.1016/j.atmosres.2023.107129, 2024.

Kafle, D. N. and Coulter, R. L.: Micropulse lidar-derived aerosol optical depth climatology at ARM sites world-wide, J. Geophys. Res.-Atmos., 118, 7293–7308, https://doi.org/10.1002/jgrd.50536, 2013.

Kanji, Z.A., Ladino, L.A., Wex, H.K., Boose, Y., Burkert-Kohn, M., Cziczo, D.J., Krämer, M.: Overview of ice nucleating particles, Meteorol. Monogr., 58, 1.1–1.33, https://doi.org/10.1175/AMSMONOGRAPHS-D-16-0006.1, 2017.

Kanamitsu, M.: Description of the NMC global data assimilation and forecast system, Weather Forecast., 4, 335–342, https://doi.org/10.1175/1520-0434(1989)004<0335:DOTNGD>2.0.CO;2, 1989.

Kim, M.-H., Omar, A. H., Tackett, J. L., Vaughan, M. A., Winker, D. M., Trepte, C. R., Hu, Y., Liu, Z., Poole, L. R., Pitts, M. C., Kar, J., and Magill, B. E.: The CALIPSO version 4 automated aerosol classification and lidar ratio selection algorithm, Atmos. Meas. Tech., 11, 6107–6135, https://doi.org/10.5194/amt-11-6107-2018, 2018.

Kong, W. and Yi, F.: Convective boundary layer evolution from lidar backscatter and its relationship with surface aerosol concentration at a location of a central China megacity, J. Geophys. Res.-Atmos, 120, 7928–7940. https://doi.org/10.1002/2015JD023248, 2015.

Lee, J., Hsu, N. C., Bettenhausen, C., Sayer, A. M., Seftor, C. J., and Jeong, M. J.: Retrieving the height of smoke and dust aerosols by synergistic use of VIIRS, OMPS, and CALIOP observations, J. Geophys. Res.-Atmos., 120, 8372-8388, https://doi.org/10.1002/2015JD023567, 2015.

Li, Y., Sun, J.X., Bi, Y.H., Wang, Q.Q., Zhao, X.J., Lei, L., Du, A.D., Li, Z.J., Wang, Z.F., Pan, X.L., Han, C.Z, and Sun, Y.L.: New insights into scavenging effect of aerosol species during summer rainfall process in Beijing, J. Geophys. Res.-Atmos. 128, e2023JD038642, https://doi.org/10.1029/2023JD038642, 2023.

Liu, M., Huang, X., Song, Y., Xu, T., Wang, S., Wu, Z., Hu, M., Zhang, L., Zhang, Q., Pan, Y., Liu, X., and Zhu, T.: Rapid SO2 emission reductions significantly increase tropospheric ammonia concentrations over the North China Plain, Atmos. Chem. Phys., 18, 17933–17943, https://doi.org/10.5194/acp-18-17933-2018, 2018.

Liu, F., Yi, F., Zhang, Y., and Yi, Y.: Double-receiver-based pure rotational Raman LiDAR for measuring atmospheric temperature at altitudes between near ground and up to 35 km, IEEE Trans. Geosci. Remote Sens., 57, 10301–10309, https://doi.org/10.1109/TGRS.2019.2933461, 2019.

https://doi.org/10.5194/egusphere-2025-56
Preprint. Discussion started: 10 February 2025

Liu, M. and Matsui, H.: Aerosol radiative forcings induced by substantial changes in anthropogenic emissions in China from 2008 to 2016, Atmos. Chem. Phys., 21, 5965–5982, https://doi.org/10.5194/acp-21-5965-2021, 2021.

Lolli, S., Sicard, M., Amato, F., Comeron, A., Gíl-Diaz, C., Landi, T. C., Munoz-Porcar, C., Oliveira, D., Dios Otin, F., Rocadenbosch, F., Rodriguez-Gomez, A., Alastuey, A., Querol, X., and Reche, C.: Climatological assessment of the vertically resolved optical and microphysical aerosol properties by lidar measurements, sun photometer, and in situ observations over 17 years at Universitat Politècnica de Catalunya (UPC) Barcelona, Atmos. Chem. Phys., 23, 12887-12906, https://doi.org/10.5194/acp-23-12887-2023, 2023.

Lu, X., Mao, F., Pan, Z., Gong, W., Wang, W., Tian, L., and Fang, S.: Three-dimensional physical and optical characteristics of aerosols over Central China from long-term CALIPSO and HYSPLIT data, Remote Sens., 10, 314, https://doi.org/10.3390/rs10020314, 2018.

Mamouri, R.E., Ansmann, A., Nisantzi, A., Kokkalis, P., Schwarz, A., and Hadjimitsis, D.: Low Arabian extinction-to-backscatter ratio, Geophys. Res. Lett., 40, 4762-4766. https://doi.org/10.1002/grl.50898, 2013.

Mamouri, R.E. and Ansmann, A.: Potential of polarization lidar to provide profiles of CCN- and INP-relevant aerosol parameters, Atmos. Chem. Phys., 16, 5905-5931, https://doi.org/10.5194/acp-16-5905-2016, 2016.

Mamouri, R.E. and Ansmann, A.: Potential of polarization/Raman lidar to separate fine dust, coarse dust, maritime, and anthropogenic aerosol profiles, Atmos. Meas. Tech., 10, 3403–3427, https://doi.org/10.5194/amt-10-3403-2017, 2017.

Miao, Y., and Liu, S.: Linkages between aerosol pollution and planetary boundary layer structure in China, Sci. Total Environ., 650, 288–296, https://doi.org/10.1016/j.scitotenv.2018.09.032, 2019.

Miri, R., Pujol, O., Hu, Q., Goloub, P., Veselovskii, I., Podvin, T., and Ducos, F.: Innovative aerosol hygroscopic growth study from Mie–Raman–fluorescence lidar and microwave radiometer synergy, Atmos. Meas. Tech., 17, 3367–3375, https://doi.org/10.5194/amt-17-3367-2024, 2024.

MODIS: Moderate Resolution Imaging Spectroradiometer, daily reflectance images from NASA Worldview, NASA, [data set] https://worldview.earthdata.nasa.gov/ (last access: 20 November 2024), 2025.

Nash, J., Oakley, T., Vömel, H., and Li, W.: WMO intercomparison of high quality radiosonde systems, Yangjiang, China (vol. 107, p.238). Geneva, Switzerland: World Meteorological Organization, Instruments and Observing Methods, 2011.

OMPS: Ozone Mapping and Profiler Suite, EarthData [data set], https://www.earthdata.nasa.gov/sensors/omps/ (last access: 12 November 2024), 2025.

Pan, X., Yi, F., Liu, F., Zhang, Y., and Yan, Y.: Diurnal temperature variations in the lower troposphere as measured by an all-day-operational pure rotational Raman lidar, Appl. Opt., 59, 8688–8696, https://doi.org/10.1364/AO.394484, 2020.

Papachristopoulou, K., Raptis, I.-P., Gkikas, A., Fountoulakis, I., Masoom, A., and Kazadzis, S.: Aerosol optical depth regime over megacities of the world, Atmos. Chem. Phys., 22, 15703-15727, https://doi.org/10.5194/acp-22-15703-2022, 2022.

Peng, L., Yi, F., Liu, F., Yin, Z., and He, Y.: Optical properties of aerosol and cloud particles measured by a single-line-extracted pure rotational Raman lidar, Opt. Express, 29, 21947–21964, https://doi.org/10.1364/OE.427864, 2021.

https://doi.org/10.5194/egusphere-2025-56
Preprint. Discussion started: 10 February 2025

Peng, S., Yang, Q., Shupe, M. D., Xi, X., Han, B., Chen, D., Dahlke, S., and Liu, C.: The characteristics of atmospheric boundary layer height over the Arctic Ocean during MOSAiC, Atmos. Chem. Phys., 23, 8683–8703, https://doi.org/10.5194/acp-23-8683-2023, 2023.

Rosenfeld, D., Andreae, M.O., Asmi, A., Chin, M., de Leeuw, G., Donovan, D.P., Kahn, R., Kinne, S., Kivekäs, N., Kulmala, M., Lau, W., Schmidt, K. S., Suni, T., Wagner, T., Wild, M., and Quaas, J.: Global observations of aerosol-cloud-precipitation-climate interactions, Rev. Geophys., 52, 750–808. https://doi.org/10.1002/2013RG000441, 2014.

Stein, A. F., Draxler, R. R., Rolph, G. D., Stunder, B. J., Cohen, M. D., and Ngan, F.: NOAA's HYSPLIT atmospheric transport and dispersion modeling system, B. Am. Meteorol. Soc., 96, 2059–2077, https://doi.org/10.1175/BAMS-D-14-00110.1, 2015.

Sun, D.Q., Ge, Y., and Zhou, Y.H.: Punishing and rewarding: how do policy measures affect crop straw use by farmers? An empirical analysis of Jiangsu Province of China, Energy Policy, 134, 110882. https://doi.org/10.1016/j.enpol.2019.110882, 2019.

Tan, W., Li, C., Liu, Y., Meng, X., Wu, Z., Kang, L., and Zhu, T.: Potential of polarization lidar to profile the urban aerosol phase state during haze episodes, Environ. Sci. Technol. Lett., 7, 54–59, https://doi.org/10.1021/acs.estlett.9b00695, 2019.

Tao, M., Chen, L., Wang, J., Wang, L., Wang, W., Lin, C., Gui, L., Wang, L., Yu, C., and Wang, Y.: Characterization of dust activation and their prevailing transport over East Asia based on multi-satellite observations, Atmos. Res., 265, 105886, https://doi.org/10.1016/j.atmosres.2021.105886, 2022.

The State Council of the People's Republic of China: Action Plan on Air Pollution Prevention and Control, available at: https://www.gov.cn/zwgk/2013-09/12/content_2486773.htm (last access: 26 November 2024), 2013 (in Chinese).

The State Council of the People's Republic of China: Three-year Plan on Defending the blue sky, available at: https://www.gov.cn/gongbao/2023/issue_10886/202312/content_6921385.html (last access: 5 January 2025), 2023 (in Chinese).

The State Council of the People's Republic of China: Action Plan for continuous improvement of air quality, available at: https://www.gov.cn/zhengce/content/2018-07/03/content_5303158.htm (last access: 12 December 2024), 2023 (in Chinese).

Tong, P.F., Chen, S.X., and Tang, C.Y.: Detecting and evaluating dust-events in North China with ground air quality data, Earth Space Sci., 9., e2021EA001849, https://doi.org/10.1029/2021EA001849, 2022.

van Donkelaar, A., Martin, R.V., Brauer, M., Boys, B.L.: Use of satellite observations for long-term exposure assessment of global concentrations of fine particulate matter, Environ. Health Perspect., 123, 135–143. https://doi.org/10.1289/ehp.1408646, 2015.

Wang, L., Xin, J., Li, X., Wang, Y.: The variability of biomass burning and its influence on regional aerosol properties during the wheat harvest season in North China, Atmos. Res., 157, 153–163, https://doi.org/10.1016/j.atmosres.2015.01.009, 2015.

https://doi.org/10.5194/egusphere-2025-56
Preprint. Discussion started: 10 February 2025

675 Wang, Y., Chen, Y., Wu, Z. J., Shang, D. J., Bian, Y.X., Du, Z. F., Schmitt, S. H., Su, R., Gkatzelis, G. I., Schlag, P., Hohaus, T., Voliotis, A., Lu, K. D., Zen, L. M., Zhao, C. S., Alfarra, M. R., Mcfiggans, G., Wiedensohler, A., Kiendler-Scharr, A., Zhang, Y. H., Hu, M.: Mutual promotion between aerosol particle liquid water and particulate nitrate enhancement leads to severe nitrate-dominated particulate matter pollution and low visibility, Atmos. Chem. Phys., 20, 2161–2175. https://doi.org/10.5194/acp-20-2161-2020, 2020.

680 Wang, S., Yin, C., Li, F., and Richel, A.: Innovative incentives can sustainably enhance the achievement of straw burning control in China, Sci. Total Environ., 857, 159498, https://doi.org/10.1016/j.scitotenv.2022.159498, 2023.

Winker, D.M., Pelon, J., Coakley Jr., J.A., Ackerman, S.A., Charlson, R.J., Colarco, P.R., Flamant, P., Fu, Q., Hoff, R.M., Kittaka, C., Kubar, T.L., Le Treut, H., McCormick, M. P., M´egie, G., Poole, L., Powell, K., Trepte, C., Vaughan, M.A., and Wielicki, B.A.: The CALIPSO mission: a global 3D view of aerosols and clouds, Bull. Am. Meteorol. Soc., 91, 1211–

685 1230. https://doi.org/10.1175/2010BAMS3009.1, 2010.

Wu, W., Zha, Y., Zhang, J., Gao, J., and He, J.: A temperature inversion-induced air pollution process as analyzed from Mie LiDAR data, Sci. Total Environ., 479, 102–108, https://doi.org/10.1016/j.scitotenv.2014.01.112, 2014.

Wu, Y., Han, Y., Voulgarakis, A., Wang, T., Li, M., Wang, Y., Xie, M., Zhuang, B., and Li, S.: An agricultural biomass burning episode in eastern China: Transport, optical properties, and impacts on regional air quality, J. Geophys. Res.-

690 Atmos., 122, 2304–2324, https://doi.org/10.1002/2016JD025319, 2017.

Xie, R., Sabel, C.E., Lu, X., Zhu, W., Kan, H., Nielsen, C.P., Wang, H.: Long-term trend and spatial pattern of PM2.5 induced premature mortality in China, Environ. Int., 97, 180–186, https://doi.org/10.1016/j.envint.2016.09.003, 2016.

Xu, X., Levy, J.K., Zhaohui, L., and Hong, C.: An investigation of sand–dust storm events and land surface characteristics in China using NOAA NDVI data, Glob. Planet. Chang., 52, 182–196. https://doi.org/10.1016/j.gloplacha.2006.02.009,

695 2006.

Xu, Q., Wang, S., Jiang, J., Bhattarai, N., Li, X., Chang, X., Qiu, X., Zheng, M., Hua, Y., and Hao, J.: Nitrate dominates the chemical composition of PM2.5 during haze event in Beijing, China, Sci Total Environ., 689, 1293–1303, https://doi.org/10.1016/j.scitotenv.2019.06.294, 2019.

Yi, Y., Yi, F., Liu, F., Zhang, Y., Yu, C., and He, Y.: Microphysical process of precipitating hydrometeors from warm-front

700 mid-level stratiform clouds revealed by ground-based lidar observations, Atmos. Chem. Phys., 21, 17649–17664, https://doi.org/10.5194/acp-21-17649-2021, 2021.

Yi, F., Yu, C., Zhang, Y., Liu, F., Yi, Y., He, Y., Yin, Z., Zhou, J.: Pure rotational Raman lidar for accurate profiling of atmospheric temperature and aerosol/cloud backscatter coefficients, Opt. Express, 32, 45566–45581, https://doi.org/10.1364/OE.539628, 2024.

705 Yin, Z., Yi, F., He, Y., Liu, F., Yu, C., Zhang, Y., and Wang, W.: Asian dust impacts on heterogeneous ice formation at Wuhan based on polarization lidar measurements, Atmos. Environ., 246, 118166, https://doi.org/10.1016/j.atmosenv.2020.118166, 2021a.

https://doi.org/10.5194/egusphere-2025-56
Preprint. Discussion started: 10 February 2025

Yin, Z., Yi, F., Liu, F., He, Y., Zhang, Y., Yu, C., and Zhang, Y.: Long-term variations of aerosol optical properties over Wuhan with polarization lidar, Atmos. Environ., 259, 118508, https://doi.org/10.1016/j.atmosenv.2021.118508, 2021b.

Zeng, H., Xiao, C., Chen, X., Chen, Y., and Ye, D.: State of China's climate in 2019, Atmos. Ocean. Sci. Lett., 13, 356-362, https://doi.org/10.1080/16742834.2020.1762159, 2020.

Zha, S., Zhang, S., Cheng, T., Chen, J., Huang, G., Li, X., and Wang, Q. F.: Agricultural Fires and Their Potential Im pacts on Regional Air Quality over China, Aerosol Air Qual. Res., 13, 992–1001, https://doi.org/10.4209/aaqr.2012.10.0277, 2013.

Zhang, D., Zakey, A.S., Gao, X.J., Giorgi, F., and Solmon, F.: Simulation of dust aerosol and its regional feedbacks over East Asia using a regional climate model, Atmos. Chem. Phys., 9, 1095–1110, https://doi.org/10.5194/acp-9-1095-2009, 2009.

Zhang, M., Ma, Y., Gong, W., and Zhu, Z: Aerosol optical properties of a haze episode in Wuhan based on ground-based and satellite observations, Atmosphere 5, 699–719, https://doi.org/10.3390/atmos5040699, 2014.

Zhang, F., Wang, Z., Cheng, H., Lv, X., Gong, W., Wang, X., and Zhang, G.: Seasonal variations and chemical characteristics of PM25 in Wuhan, central China, Sci. Total Environ., 518–519, 97–105, https://doi.org/10.1016/j.scitotenv.2015.02.054, 2015.

Zhang Q, Zheng Y, Tong D, Shao M, Wang S, Zhang Y, Xu, X., Wang, J., He, H., Liu, W., Ding, Y., Lei, Y., Li, J., Wang, Z., Zhang, X., Wang, Y., Cheng, J., Liu, Y., Shi, Q., Yan, L., Geng, G., Hong, C., Li, M., Liu, F., Zheng, B., Cao, J., Ding, A., Gao, J., Fu, Q., Huo, J., Liu, B., Liu, Z., Yang, F., He, K., and Hao, J.: Drivers of improved $PM_{2.5}$ air quality in China from 2013 to 2017, Proc. Natl. Acad. Sci. U. S. A., 22: 24463–24469, https://doi.org/10.1073/pnas.1907956116, 2019.

Zhang, Y., Zhang, Y., Yu, C., and Yi, F.: Evolution of aerosols in the atmospheric boundary layer and elevated layers during a severe, persistent haze episode in a central China megacity, Atmosphere, 12, 152, https://doi.org/10.3390/atmos12020152, 2021a.

Zhang, Y., Yin, Z., Wang, H. and He, S: 2020/21 record-breaking cold waves in east of China enhanced by the 'Warm Arctic-Cold Siberia' pattern, Environ. Res. Lett., 16, 094040. https://doi.org/10.1088/1748-9326/ac1f46, 2021b.

Zhang, X., Li, L., Che, H., Dubovik, O., Derimian, Y., Holben, B., Gupta, P., Eck, T.F., Lind, E.S., Toledano, C., Xia, X., Zheng, Y., Gui, K., and Zhang, X.: Aerosol components derived from global AERONET measurements by GRASP: a new value-added aerosol component global dataset and its application, Bull. Am. Meteorol. Soc., 105, E1822–E1848, https://doi.org/10.1175/BAMS-D-23-0260.1, 2024.

Zheng, B., Tong, D., Li, M., Liu, F., Hong, C., Geng, G., Li, H., Li, X., Peng, L., Qi, J., Yan, L., Zhang, Y., Zhao, H., Zheng, Y., He, K., and Zhang, Q.: Trends in China's anthropogenic emissions since 2010 as the consequence of clean air actions, Atmos. Chem. Phys., 18, 14095–14111, https://doi.org/10.5194/acp-18-14095-2018, 2018.

Zhuang, J. and Yi, F.: Nabro aerosol evolution observed jointly by lidars at a midlatitude site and CALIPSO, Atmos. Environ., 140, 106–116, https://doi.org/10.1016/j.atmosenv.2016.05.048, 2016.

https://doi.org/10.5194/egusphere-2025-56
Preprint. Discussion started: 10 February 2025

740 Zieger, P., Fierz-Schmidhauser, R., Weingartner, E., and Baltensperger, U.: Effects of relative humidity on aerosol light scattering: results from different European sites, Atmos. Chem. Phys., 13, 10609–10631, https://doi.org/10.5194/acp-13-10609-2013, 2013.